astrocytes are beneficial in limiting inflammatory cell infiltration in the subacute phase of injury, before glial scar completion (33), while others have indicated that the elimination of reactive astrocytes is beneficial for SCI recovery at the subacute stage (37). Considering the above-described contradictory roles of reactive astrocytes after SCI, an ideal treatment strategy may involve inhibiting the aberrant development of hypertrophic reactive astrocytes without eliminating normal quiescent astrocytes, thus preventing a cascading wave of uncontrolled tissue damage. Based on our findings, the timing of NSC transplantation is extremely important. On the basis of our previous studies regarding glial scar formation and effective NSC migration (44), we have determined that the optimal timing of intravenous NSC injection is 7 days after injury.

Critical role of TLR-4 in the effect of NSCs expressing IFN-β

We have previously been successful at restoring functional recovery in a mouse model of SCI by using a liposome-mediated IFN-β gene delivery method (12). IFN-β is a type I IFN that exerts pleiotropic biological effects (3), and acts as a cell-cycle regulator to control the re-entrance of cells undergoing aberrant cell-cycle progression into a senescence-like state (15). Recently, it has been proven that IFNs block the constitutive activation of the MEK-ERK signaling pathway (31,38,39,48), which is activated at the site of SCI (12). IFN-β also blocks the infiltration of neutrophils and proinflammatory cytokines into sites of injury and stimulates the expression of anti-inflammatory cytokines (7). In order to clarify the novel function of IFN-β in the suppression of glial scar formation in this study, we attempted to identify the profile changes in gene expression that occur during astrocytic gliosis. This systematic processing revealed the statistically significant activation of many intriguing pathways ($p < 0.05$) (Fig. 1). Of these, the TLR-4 pathway, which plays an important role in immune regulation in astrocytes (8) and autoregulatory apoptosis in cells bearing the TLR-4 receptor (14,16), was of particular note. TLR-4 can be detected in astrocytes in sites of SCI (16). The

autoregulatory apoptosis of activated astrocytes is known to be initiated by TLR-4 and proceeds by at least 2 pathways, one of which is IFN-β activation (14). Indeed, TLR-4 ligation is essential for the autoregulatory apoptosis of cells bearing this receptor, which ultimately acts to regulate glial scar formation (16). This function requires the presence of IFN-β. Furthermore, TLR-4 deletion significantly impairs the normal progression of SCI repair and functional recovery (16). Our results demonstrate that TLR-4 inhibition results in impaired functional recovery despite the administration of F3.CD.IFN NSCs. Therefore, we can conclude from our findings that the combination of TLR-4 and IFN-β plays a crucial role in regulating post-SCI inflammation and gliosis.

Cytosine deaminase gene as a fail safe modulator of uncontrolled proliferation of NSCs

The CD gene examined in this study encodes bacterial enzyme that catalyzes the deamination of nontoxic 5-FC into the highly toxic 5-fluorouracil (FU). We have previously reported improved outcomes in animal models of brain tumors after therapy with this "suicide gene" (11,13,20,40). We therefore applied this strategy in SCI models to investigate the additive efficacy of NSC-delivered CD and IFN-β. NSCs have the ability to migrate to sites of SCI, at which they induce the apoptosis of the surrounding reactive astrocytes via the bystander effect. Thus, we anticipated that the combination of the actions of IFN-β with the 5-FC/CD-mediated bystander effect would exert greater suppression of reactive astrocytes than either treatment alone. However, this combination therapy was not found to be superior to IFN-β alone in vivo or in vitro in this study. Rather, our findings show that the addition of 5-FC to astrocytes treated with F3.CD.IFN did not cause any greater decrease in astrocyte number than treatment with F3.IFN alone. We speculate that sustained expression of IFN-β from F3.CD.IFN is required to produce an inhibitory effect in reactive astrocytes. Further, as NSCs have neuroprotective functions, including the secretion of neurotrophic factors, the presence of NSCs themselves may provide a partial explanation for functional recovery and neuroregeneration after SCI. The F3 NSC line can produce an unlimited number of

differentiated cells in vitro and in vivo, and could therefore be used in transplantation. However, serious problems could arise when transplanted NSCs proliferate uncontrollably. In order to avoid such problems, we generated an F3 human NSC line expressing both the therapeutic IFN-β gene and the CD suicide gene. The expression of CD gene provides a fail safe guard to allow removal of cells in cases of uncontrolled proliferation of grafted cells.

Noninvasive monitoring of axonal regeneration by diffusion tensor imaging

The evaluation of axonal fibers is important to assess the severity of SCI and the efficacy of treatment; however, conventional methods such as tracer injection (e.g., biotinylated dextraamine) in brain parenchyma are technically demanding and highly Invasive (27,35). Because histological examinations are required to evaluate tracer studies, it has been impossible to evaluate axonal fibers in living animals and follow the sequential growth of these axonal fibers in the same animal. In order to evaluate axonal fibers in vivo, we sought a novel method capable of noninvasive evaluation in clinical applications. With this in mind, we determined that MRI is suited for use in the assessment of the state of SCIs. Conventional T1- and T2-weighted MRI of the spinal cord only shows ambiguous images of the various spinal structures, making it difficult to identify the complicated array of directionally oriented nerve fibers. However, DTI is one of the most versatile MRI modalities for longitudinal evaluations of CNS disorders, and is capable of following the orientation of nerve fibers and tracing specific neural pathways such as the CST (19,29,32). In this study, we chose a dorsal transection model because the disruption and regeneration of axons after a transection injury can be more easily evaluated than that following a contusion injury (30,46). Because of the ability to visualize longitudinal axonal tracts in variously oriented neural fibers, DTI has tremendous potential for use in the diagnosis and evaluation of spinal cord diseases. Several researchers have reported successful DTI in the human spinal cord (4,5). To our knowledge, this is the first report of DTI-based visualization of axonal

regeneration in the spinal cord of small rodents. Significant longitudinal axonal regeneration was confirmed by DTI in F3.CD.IFN-β NSC-treated mice 4 weeks after injury.

Conclusions

In conclusion, mice that received intravenous administration of genetically engineered NSCs transduced with IFN-β gene after SCI exhibited extensive suppression of glial scar formation in the lesioned spinal cord. This effect was shown to require the expression of both TLR-4 and IFN-β. Significant neurobehavioral and electrophysiological recovery was attained, as measured by the Basso mouse scale for locomotion, inclined plane test and transcranial MEPs. Axonal regeneration was also visualized noninvasively using DTI. Our results suggest that IFN-β delivery by intravenous injection of genetically engineered NSCs inhibits glial scar formation after SCI and promotes functional recovery through the functions of TLR-4. This novel NSC-based therapy of delivering IFN-β shows promise for the treatment of patients suffering frim SCI.

Acknowledgements

This work was supported in part by grants from a Grant-in-Aid (B) for Scientific Research from the Ministry of Health, Labor, and Welfare, Japan (AN). The authors thank Dr. S. Saito, Ms. S. Shibata, Ms. C. Kajiwara and Ms. Miho Senda for their help.

References

1. Aboody, K. S.; Brown, A.; Rainov, N. G.; Bower, K.A.; Liu, S.; Yang, W.; Small, J.E.; Herrlinger, U.; Ourednik, V.; Black, P.M.; Breakefield, X.O.; Snyder, E.Y. Neural stem cells display extensive tropism for pathology in adult brain: evidence from intracranial gliomas. Proc. Natl. Acad. Sci. USA 97: 12846-12851; 2000.

2. Basso, D. M.; Fisher, L. C.; Anderson, A. J.; Jakeman, L. B.; McTigue, D. M.; Popovich, P. G. Basso Mouse Scale for locomotion detects differences in recovery after spinal cord injury in five common mouse strains. J. Neurotrauma 23: 635-659; 2006.

3. Borden, E. C.; Sen, G. C.; Uze, G.; Silverman, R. H.; Ransohoff, R. M.; Foster, G. R.; Stark, G. R. Interferons at age 50: past, current and future impact on biomedicine. Nat. Rev. Drug Discov. 6: 975-990; 2007.

4. Ducreux, D.; Lepeintre, J. F.; Fillard, P.; Loureiro, C.; Tadie, M.; Lasjaunias, P. MR diffusion tensor imaging and fiber tracking in 5 spinal cord astrocytomas. Am. J. Neuroradiol. 27: 214-216; 2006.

5. Facon, D.; Ozanne, A.; Fillard, P.; Lepeintre, J. F.; Tournoux-Facon, C.; Ducreux, D. MR diffusion tensor imaging and fiber tracking in spinal cord compression. Am. J. Neuroradiol. 26: 1587-1594; 2005.

6. Faulkner, J. R.; Herrmann, J. E.; Woo, M. J.; Tansey, K. E.; Doan, N. B.; Sofroniew, M. V. Reactive astrocytes protect tissue and preserve function after spinal cord injury. J. Neurosci. 24: 2143-2155; 2004.

7. Gok, B.; Okutan, O.; Beskonakli, E.; Palaoglu, S.; Erdamar, H.; Sargon, M .F. Effect of immunomodulation with human interferon-beta on early functional recovery from experimental spinal cord injury. Spine 32: 873-880; 2007.

8. Gorina, R.; Font-Nieves, M.; Marquez-Kisinousky, L.; Santalucia, T.; Planas, A. M. Astrocyte TLR4 activation induces a proinflammatory environment through the interplay between MyD88-dependent NF kappaB signaling, MAPK, and Jak1/Stat1 pathways. Glia 59: 242-255; 2011.

9. Hu, R.; Zhou, J.; Luo. C,; Lin, J.; Wang, X.; Li, X.; Bian, X.; Li, Y.; Wan, Q.; Yu, Y.; Feng, H. Glial scar and neuroregeneration: histological, functional, and magnetic resonance imaging

analysis in chronic spinal cord injury. J. Neurosurg. Spine 13: 169-180; 2010.

10. Hwang, D.H.; Kim, B.G.; Kim, E.J.; Lee, S.I.; Joo, I.S.; Suh, Kim. H.; Sohn, S.; Kim, S. U. Transplantation of human neural stem cells transduced with Olig2 transcription factor improves locomotor recovery and enhances myelination in the white matter of rat spinal cord following contusive injury. BMC Neurosci. 10: 117; 2009.

11. Ito, S.; Natsume, A.; Shimato, S.; Ohno, M.; Kato, T.; Chansakul, P.; Wakabayashi, T.; Kim, S. U. Human neural stem cells transduced with IFN-beta and cytosine deaminase genes intensify bystander effect in experimental glioma. Cancer Gene Ther. 17: 299-306; 2008.

12. Ito, M.; Natsume, A.; Takeuchi, H.; Shimato, S.; Ohno, M.; Wakabayashi, T.; Yoshida, J. Type I interferon inhibits astrocytic gliosis and promotes functional recovery after spinal cord injury by deactivation of the MEK/ERK pathway. J Neurotrauma 26:41-53; 2009

13. Joo, K. M.; Park, I. H.; Shin, J. Y.; Jin, J.; Kang, B.G.; Kim, M. H.; Lee, S. J.; Jo, M. Y.; Kim, S. U.; Nam, D. H. Human neural stem cells can target and deliver therapeutic genes to breast cancer brain metastases. Mol. Ther. 17: 570-575; 2009.

14. Jung, D. Y.; Lee, H.; Jung, B.Y.; Ock, J.; Lee, M. S.; Lee, W. H.; Suk, K. TLR4, but not TLR2, signals autoregulatory apoptosis of cultured microglia: a critical role of IFN-beta as a decision maker. J. Immunol. 174: 6467-6476; 2005.

15. Kaynor, C.; Xin, M.; Wakefield, J.; Barsoum, J.; Qin, X. Q. Direct evidence that IFN-beta functions as a tumor-suppressor protein. J. Interferon Cytokine Res. 22: 1089-1098, 2002.

16. Kigerl, K. A.; Lai, W.; Rivest, S.; Hart, R. P.; Satoskar, A. R.; Popovich, P. G. Toll-like receptor (TLR)-2 and TLR-4 regulate inflammation, gliosis, and myelin sparing after spinal cord injury. J. Neurochem. 102: 37-50; 2007.

17. Kim, B. G.; Kang, Y. M.; Phi, J. H.; Kim, Y. H.; Hwang, D. H.; Choi, J. Y.; Ryu, S.; Elastal, A. E.; Paek, S. H.; Wang, K. C.; Lee, S. H.; Kim, S. U.; Yoon, B. W. Implantation of polymer scaffolds seeded with neural stem cells in a canine spinal cord injury model. Cytotherapy 12: 841-845; 2010.

18. Kim, B. G.; Hwang, D. H.; Lee, S. I.; Kim, E. J.; Kim, S. U. Stem cell-based cell therapy for spinal cord injury. Cell Transplant.16: 355-364; 2007.

19. Kim, J. H.; Haldar, J.; Liang, Z. P.; Song, S. K. Diffusion tensor imaging of mouse brainstem and cervical spinal cord. J. Neurosci. Methods 176: 186-191; 2009

20. Kim, S. K.; Kim, S. U.; Park, I. H.; Bang, J. H.; Aboody, K. S.; Wang, K. C.; Cho, B. K.; Kim, M.; Menon, L. G.; Black, P. M.; Carroll, R. S. Human neural stem cells target experimental intracranial

medulloblastoma and deliver a therapeutic gene leading to tumor regression. Clin. Cancer Res. 12: 5550-5556; 2006.

21. Kim, S. U. Human neural stem cells genetically modified for brain repair in neurological disorders. Neuropathology 24: 159-171; 2004.

22. Kim, S. U. Genetically engineered human neural stem cells for brain repair in neurological diseases. Brain Dev. 29: 193-201; 2007.

23. Kim, S. U.; Park, I. H.; Kim, T. H.; Kim, K. S.; Choi, H. B.; Hong, S. H.; Bang, J. H.; Lee, M. A.; Joo, I. S.; Lee, C. S.; Kim, Y. S. Brain transplantation of human neural stem cells transduced with tyrosine hydroxylase and GTP cyclohydrolase 1 provides functional improvement in animal models of Parkinson disease. Neuropathology 26: 129-140; 2006.

24. Kim, S. U. Neural stem cell-based gene therapy for brain tumors. Stem Cell Rev 7:130-140; 2010.

25. Kim, S. U.; de, Vellis. J. Stem cell-based cell therapy in neurological diseases: a review. J. Neurosci. Res. 87: 2183-2200; 2009.

26. Lacroix, S.; Havton, L. A.; McKay, H.; Yang, H.; Brant, A.; Roberts, J.; Tuszynski, M. H. Bilateral corticospinal projections arise from each motor cortex in the macaque monkey: a quantitative study. J. Comp. Neurol. 473: 147-161; 2004.

27. Lee, H. J.; Kim, K. S.; Kim, E. J.; Choi, H. B.; Lee, K. H.; Park, I. H.; Ko, Y.; Jeong, S. W.; Kim, S. U. Brain transplantation of immortalized human neural stem cells promotes functional recovery in mouse intracerebral hemorrhage stroke model. Stem Cells 25: 1204-1212; 2007.

28. Lee, J. S.; Han, M. K.; Kim, S. H.; Kwon, O. K.; Kim, J. H. Fiber tracking by diffusion tensor imaging in corticospinal tract stroke: Topographical correlation with clinical symptoms. Neuroimage 26: 771-776; 2005.

29. Lee, S. I.; Kim, B. G.; Hwang, D. H.; Kim, H. M.; Kim, S. U. Overexpression of Bcl-XL in human neural stem cells promotes graft survival and functional recovery following transplantation in spinal cord injury. J. Neurosci. Res. 87: 3186-3197; 2009.

30. Levi, A. D.; Dancausse, H.; Li, X.; Duncan, S.; Horkey, L.; Oliviera, M. Peripheral nerve grafts promoting central nervous system regeneration after spinal cord injury in the primate. J. Neurosurg. 96: 197-205; 2002.

31. Li, C.; Chi, S.; He, N.; Zhang, X.; Guicherit, O.; Wagner, R.; Tyring, S.; Xie, J. IFNalpha induces Fas expression and apoptosis in hedgehog pathway activated BCC cells through inhibiting Ras-Erk signaling. Oncogene 23: 1608-1617; 2004.

32. Masutani, Y.; Aoki, S.; Abe, O.; Hayashi, N.; Otomo, K. MR diffusion tensor imaging: recent advance and new techniques for diffusion tensor visualization. Eur. J. Radiol. 46: 53-66; 2003.

33. Okada, S.; Nakamura, M.; Katoh, H.; Miyao, T.; Shimazaki, T.; Ishii, K.; Yamane, J.; Yoshimura, A.; Iwamoto, Y.; Toyama, Y.; Okano, H. Conditional ablation of Stat3 or Socs3 discloses a dual role for reactive astrocytes after spinal cord injury. Nat. Med. 12: 829-834; 2006.

34. Pajevic, S.; Pierpaoli, C. Color schemes to represent the orientation of anisotropic tissues from diffusion tensor data: application to white matter fiber tract mapping in the human brain. Magn. Reson. Med. 42: 526-540; 1999.

35. Ralston, D. D.; Ralston, H. J. The terminations of corticospinal tract axons in the macaque monkey. J. Comp. Neurol. 242: 325-337; 1985.

36. Rivlin, A. S.; Tator, C. H. Objective clinical assessment of motor function after experimental spinal cord injury in the rat. J. Neurosurg. 47: 577-581; 1977.

37. Rolls, A.; Shechter, R.; Schwartz, M. The bright side of the glial scar in CNS repair. Nat. Rev. Neurosci. 10: 235-241; 2009.

38. Romerio, F.; Riva, A.; Zella, D. Interferon-alpha2b reduces phosphorylation and activity of MEK and ERK through a Ras/Raf-independent mechanism. Brit. J. Cancer 83: 532-538; 2000.

39. Romerio, F.; Zella, D. MEK and ERK inhibitors enhance the anti-proliferative effect of interferon-alpha2b. FASEB J. 16: 1680-1682; 2002.

40. Shimato, S.; Natsume, A.; Takeuchi, H.; Wakabayashi, T.; Fujii, M.; Ito, M.; Ito, S.; Park, I. H.; Bang, J. H.; Kim, S. U.; Yoshida, J. Human neural stem cells target and deliver therapeutic gene to experimental leptomeningeal medulloblastoma. Gene Ther. 14: 1132-1142; 2007.

41. Stejskal, E.; Tanner, J. Spin Diffusion Measurements: Spin Echoes in the Presence of a Time-Dependent Field Gradient. J. Chem. Phys. 42: 288-292; 1965.

42. Stichel, C. C.; Muller, H. W. The CNS lesion scar: new vistas on an old regeneration barrier. Cell Tissue Res. 294: 1-9; 1998.

43. Suzuki, H.; Fukuyama, R.; Hasegawa, Y.; Tamaki, T.; Nishio, M.; Nakashima, T.; Tatematsu, M. Tumor thickness, depth of invasion, and Bcl-2 expression are correlated with FDG-uptake in oral squamous cell carcinomas. Oral Oncol. 45: 891-897; 2009.

44. Takeuchi, H.; Natsume, A.; Wakabayashi, T.; Aoshima, C.; Shimato, S.; Ito, M.; Ishii, J.; Maeda, Y.; Hara, M.; Kim, S. U.; Yoshida, J. Intravenously transplanted human neural stem cells migrate to the injured spinal cord in adult mice in an SDF-1- and HGF-dependent manner. Neurosci. Lett. 426: 69-74; 2007.

45. Tang, B. L.; Low, C. B. Genetic manipulation of neural stem cells for transplantation into the injured spinal cord. Cell Mol. Neurobiol. 27: 75-85; 2007.

46. Tuszynski, M. H.; Grill, R.; Jones, L. L.; McKay, H. M.; Blesch, A. Spontaneous and augmented growth of axons in the primate spinal cord: effects of local injury and nerve growth factor-secreting cell grafts. J. Comp. Neurol. 449: 88-101; 2002.

47. Yasuhara, T.; Matsukawa, N.; Hara, K.; Yu, G.; Xu, L.; Maki, M.; Kim, S. U.; Borlongan CV Transplantation of human neural stem cells exerts neuroprotection in a rat model of Parkinson's disease. J. Neurosci. 26: 12497-12511; 2006.

48. Zella, D.; Romerio, F.; Curreli, S.; Secchiero, P.; Cicala, C.; Zagury, D.; Gallo, R. C. IFN-alpha 2b reduces IL-2 production and IL-2 receptor function in primary CD4+ T cells. J. Immunol. 164: 2296-2302; 2000.

Figure legends

Figure 1. (A) Significantly activated pathways at glial scar following spinal cord injury. (B) Toll-like receptor-4 is markedly upregulated in the lesioned astrocytes. pAS, primary cultured astrocytes; nSC, normal spinal cord; SCI-glia, glial scar in spinal cord injury.

Figure 2. F3 human neural stem cells migrate to mouse spinal cord injury (SCI) lesion site. (A) A hematoxilin and eosin stained section shows that a large number of transplanted neural stem cells infiltrated in the lesioned site. (B) Fluorescence microscopy reveals a large number of DiI-labeled F3 cells at the lesion site. (C) Immunohistochemical staining with anti-β-galactosidase (β-gal) antibody demonstrates that β-gal-positive cells are extensively distributed in the lesioned area of a mouse injected with F3 cells expressing β-gal (F3.LacZ). (D) Higher magnification of panel C. (E) A control injured animal injected with PBS alone; none of β-gal-positive cells are observed in the spinal cord. (F) Higher magnification of panel E. (G) IFN-β mRNA expression is detected at the SCI site of the animals injected with F3.CD.IFN-β neural stem cells by RT-PCR. F3.CD.IFN:positive control; SCI/F3.CD.IFN: SCI site of an animal injected with F3.CD.IFN-β cells; SCI, SCI site of an animal injected with PBS only.

Figure 3. F3.CD.IFN-β cells inhibit growth of primary normal astrocytes. Astrocytes were co-cultured with either F3.LacZ or F3.CD.IFN-β cells (F3.CD.IFN) at various ratios of astrocytes to F3 cells (1:0, 20:1, and 40:1). (A) Immunofluorescence images of primary astrocytes alone or co-culture (astrocyte:F3 ratio, 40:1) of astrocytes and F3.LacZ, F3.CD.IFN or F3.CD.IFN + 5FC, respectively. Green cells and red cells indicate GFAP-positive astrocytes and DiI-labeled F3 cells, respectively. (B) Subsequently, cells were immunostained with anti-GFAP antibody, and the total numbers of GFAP-positive cells were counted. The number of astrocytes decreased significantly in F3.CD.IFN group. * $P < 0.05$. (C) To evaluate whether TLR-4 is necessary for IFN-β to exert this inhibitory effect on astrocyte growth, DiI-labeled

NSCs were also co-cultured with primary astrocytes derived from TLR-4-deficient mouse in 40:1 ratio. (D) The number of TLR-4-deficient astrocytes did not change.

Figure 4. Intravenous administration of F3.CD.IFN-β neural stem cells spares host neural tissue and enhanced axonal regeneration.

(A) Hematoxylin and eosin stained sections of spinal cord injury sites, showing severe destruction of the dorsal half of the spinal cord above the central canal (arrow) and the formation of a granular scar at the injury site.

(B) GFAP immunohistochemical staining, showing hypertrophy of GFAP-positive reactive astrocytes even in the area ventral to the central canal. The intensity of GFAP staining is markedly decreased in the F3.CD.IFN group as compared to that in the other groups.

(C) GFAP density was calculated quantitatively using NIH imaging. * $P < 0.05$.

(D) Neurofilament (NF) immunohistochemical staining. In the PBS and F3.LacZ groups, NF-stained transverse sections demonstrate significant loss of neural fibers. In the F3.CD.IFN + 5FC group, only partial preservation of neural axons is detected. Sections from the F3.CD.IFN group reveal dramatic preservation of fiber number and alignment. (E) Quantification of NF density.*$P < 0.05$.

Figure 5. The expression of GFAP and NF at the injury site was compared in mice treated with F3.CD.IFN in the presence or absence of the TLR-4 inhibitor OxPAPC. While the dorsal half of the spinal cord was destroyed equally in every group, the anterior half of the spinal cord was found to be markedly preserved in the F3.CD.IFN group when compared to the F3.CD.IFN+OxPAPC group (A). The intensity of GFAP staining was also significantly decreased in the F3.CD.IFN group as compared to that observed in the F3.CD.IFN+OxPAPC and F3.LacZ groups (B). NF-stained transverse sections also demonstrated a significant loss of neural fibers in the F3.CD.IFN+OxPAPC and F3.LacZ groups, while neural fiber was dramatically preserved in sections from the F3.CD.IFN group (C).

Figure 6. Behavioral studies. (A) Basso mouse scale (BMS) for locomotion. We measured the recovery of hindlimb motor function in 7 mice in each treatment group. Animals were evaluated for locomotor recovery at 1, 2, 3, 4, 6, and 8 weeks after the injury. F3.CD.IFN group showed a significant improvement in BMS scores compared to the other 3 groups. Differences between the mean BMS of the F3.CD.IFN group and of the other groups were statistically significant 4 weeks after injury and thereafter (* $P < 0.05$). (B) Inclined plane test. It demonstrates significant recovery of performance 2 weeks following the injury in the F3.CD.IFN group, whereas performance of the other 3 groups remained severely impaired (* $P < 0.05$). (C, D) The improvements in the BMS scores and inclined plane test results that were observed in the F3.CD.IFN group were shown to be inhibited by the OxPAPC TLR-4 inhibitor.

Figure 7. Electrophysiology. (A) To measure signal conduction in motor pathways after SCI, transcranial electrical motor nerve evoked-action potentials (MEPs) were measured at 4 and 8 weeks after injury. Animals in the F3.CD.IFN group showed significantly better recovery at both 4 and 8 weeks after injury (* $P < 0.05$). (B) OxPAPC administration in the F3.CD.IFN group significantly worsened the mean MEP amplitude to 178 μV and 228 μV at 4 and 8 weeks, respectively ($p < 0.05$).

Figure 8. Assessment of regenerative sprouting of CST axons by 7-T MRI. Four weeks after dorsal hemisection. MRI (DTI) was performed in mice receiving PBS, F3.LacZ, or F3.CD.IFN. Diffusion tensor of the thoracic spinal cord was visualized. The eigenvectors associated with the tract was depicted as colors according to its orientation; blue illustrates a longitudinal (superior-inferior) orientation. Continuity of this longitudinal tract demonstrated functional regeneration of the axons. In the PBS and F3.LacZ groups, the injury site (arrow) and its surrounding area display high intensity in T2-weighted sagittal sections (arrow

heads), indicating spinal cord edema or necrotic tissue alteration, whereas high intensity is not detected in the F3.CD.IFN group. DTI of the injured spinal cord in the PBS and F3.LacZ groups reveals discontinuity of longitudinal fibers, while these fibers were mostly visible in the F3.CD.IFN group.

A

Map	Map Folders	Cell process
Regulation of CDC42 activity	Function groups/G-proteins/RAS-group	small GTPase mediated signal transduction
TGF-beta receptor signaling	Cell signaling/Growth and differentiation/Growth and differentiation (common pathways) Function groups/Growth factors	intracellular receptor-mediated signaling pathway, response to extracellular stimulus
Cell-matrix glycoconjugates	Cell signaling/Cell adhesion	cell adhesion
The metaphase checkpoint	Cell signaling/Cell cycle control	cell cycle
IL1 signaling pathway	Cell signaling/Immune response Function groups/Cyto/chemokines	cytokine and chemokine mediated signaling pathway, immune response
Transcription regulation of granulocyte development	Cell signaling/Growth and differentiation/Hematopoiesis	response to extracellular stimulus
Toll-like receptor (TLR) ligands and common TLR signaling pathway leading to cell proinflammatory response	Cell signaling/Immune response	immune response

B

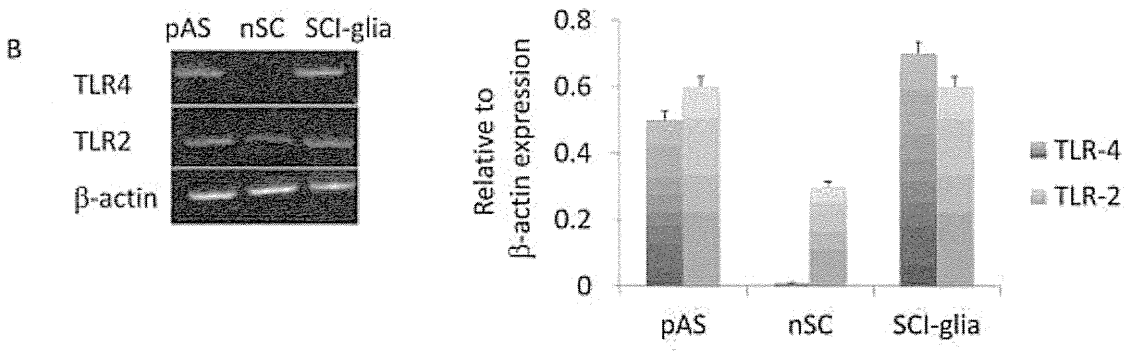

Figure 1

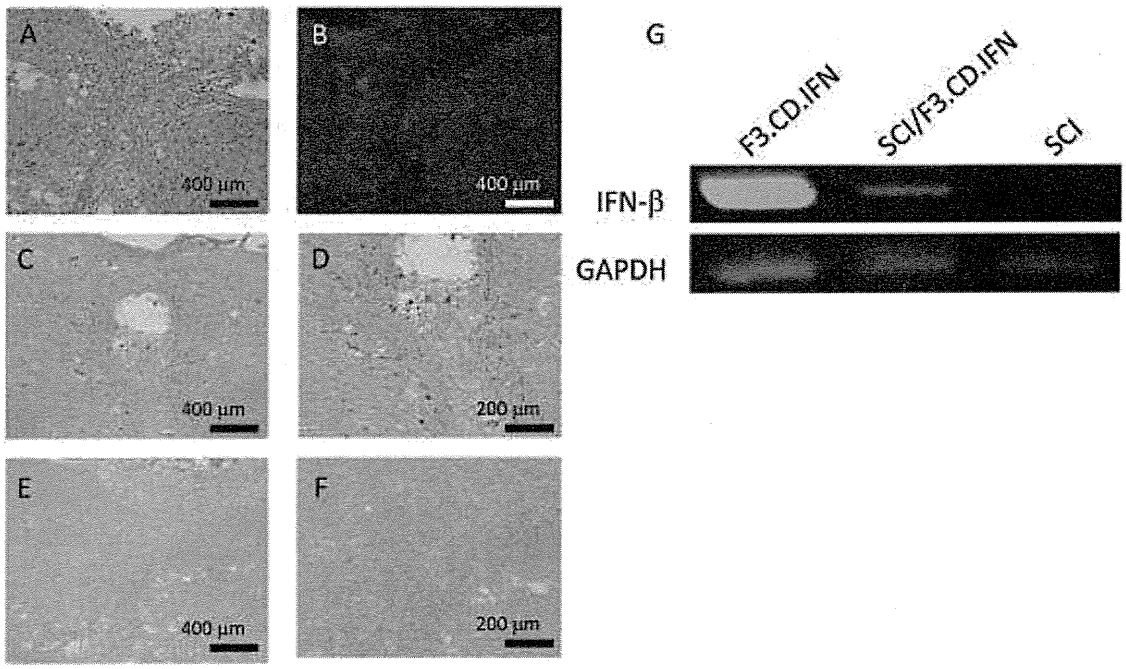

Figure 2

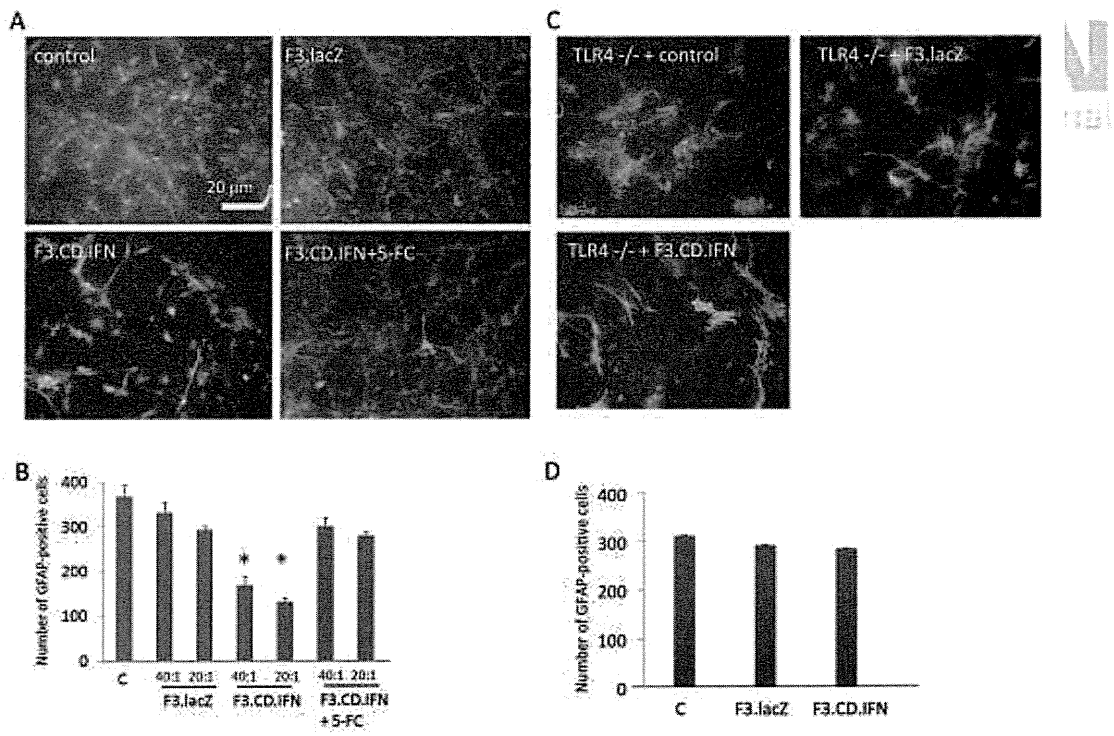

Figure 3

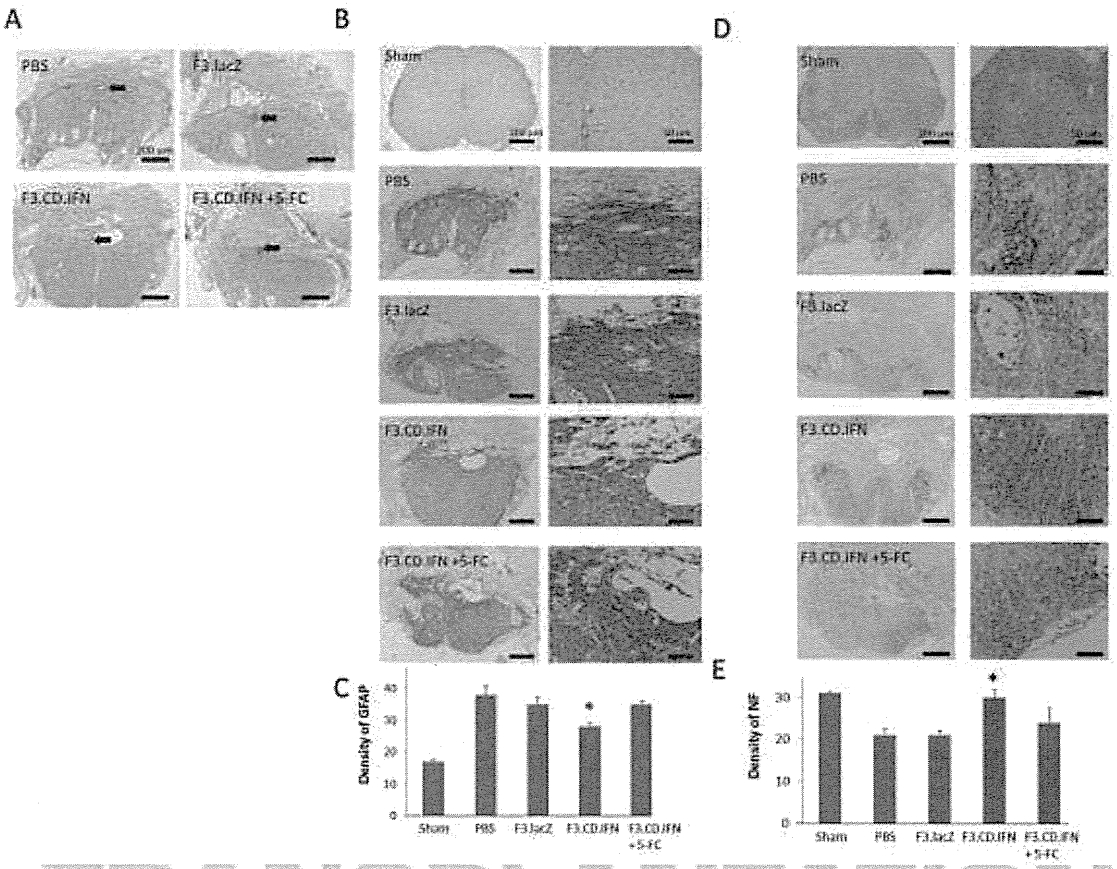

Figure 4

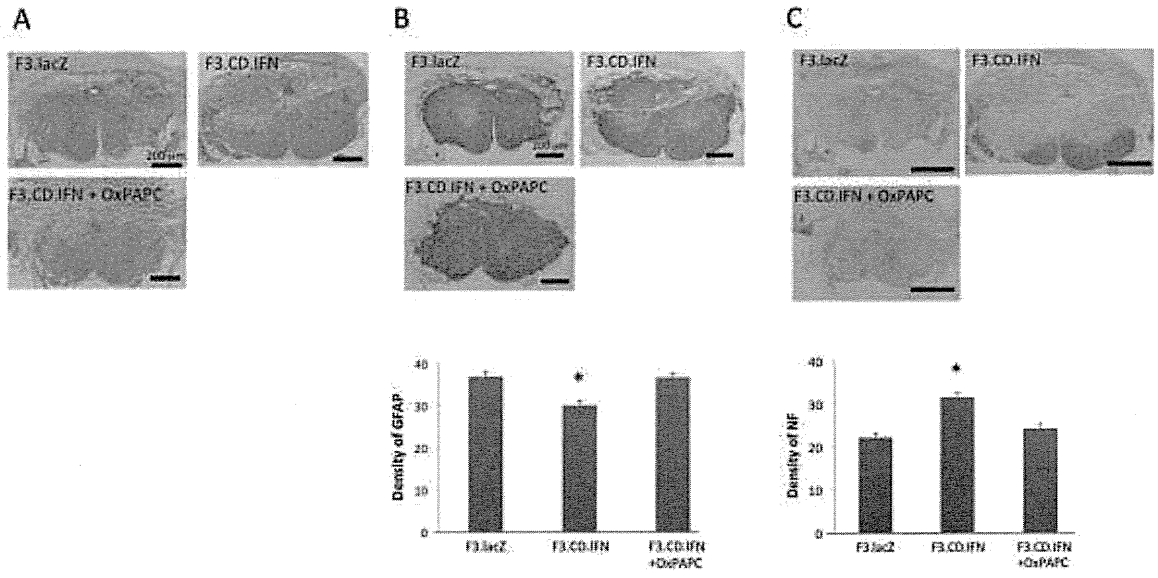

Figure 5

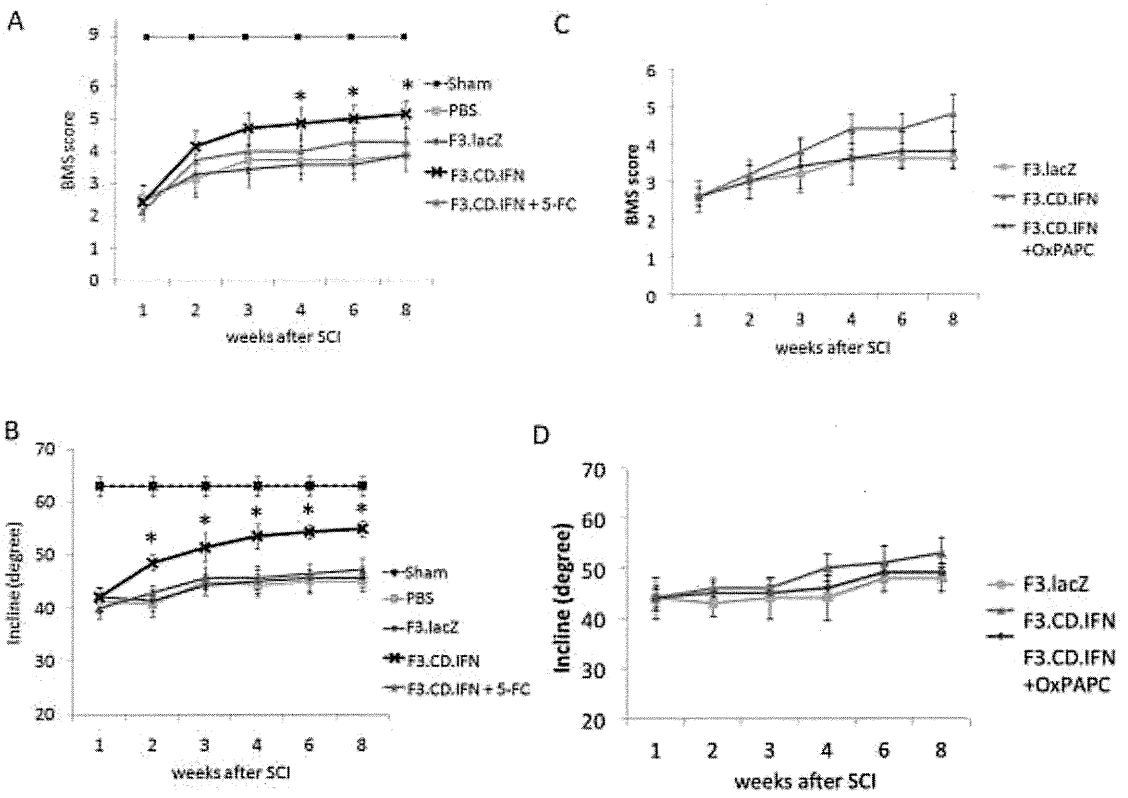

Figure 6

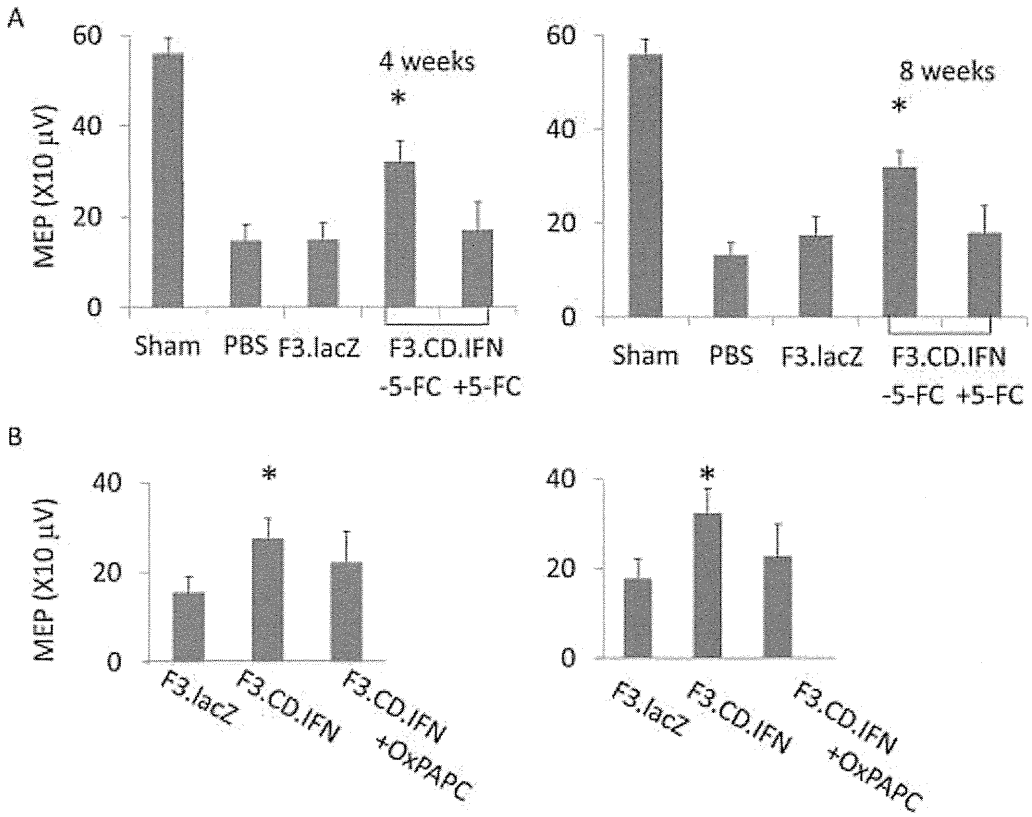

Figure 7

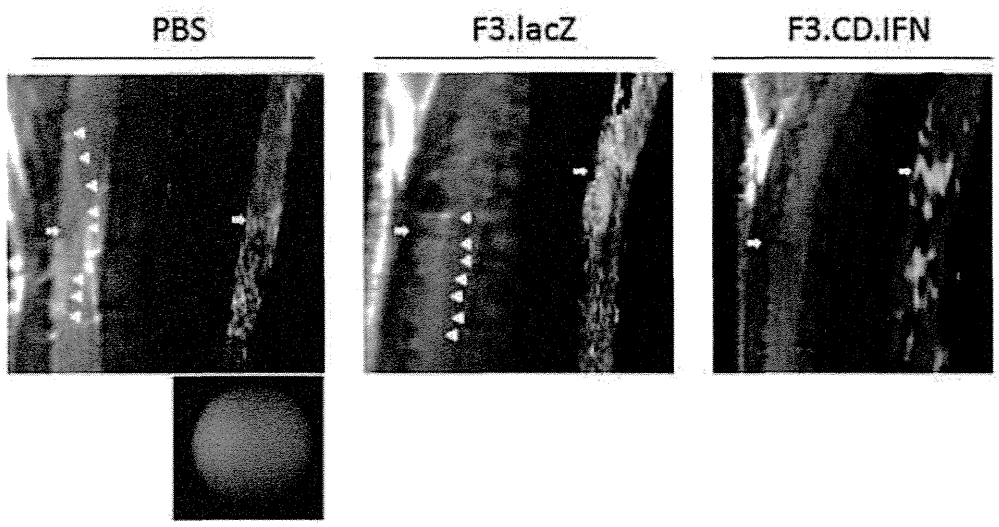

Figure 8

Biomaterials 34 (2013) 492–500

Contents lists available at SciVerse ScienceDirect

Biomaterials

journal homepage: www.elsevier.com/locate/biomaterials

Gd-DTPA-loaded polymer–metal complex micelles with high relaxivity for MR cancer imaging

Peng Mi [a], Horacio Cabral [a], Daisuke Kokuryo [b], Mohammad Rafi [c], Yasuko Terada [d], Ichio Aoki [b], Tsuneo Saga [b], Ishii Takehiko [a], Nobuhiro Nishiyama [c,**], Kazunori Kataoka [a,c,e,*]

[a] Department of Bioengineering, Graduate School of Engineering, The University of Tokyo, 7-3-1 Hongo, Bunkyo-ku, Tokyo 113-8656, Japan
[b] Molecular Imaging Center, National Institute of Radiological Sciences, Anagawa 4-9-1, Inage, Chiba 263-8555, Japan
[c] Center for Disease Biology and Integrative Medicine, Graduate School of Medicine, The University of Tokyo, 7-3-1 Hongo, Bunkyo-ku, Tokyo 113-0033, Japan
[d] SPring 8, JASRI, 1-1-1 Kouto, Sayo-cho, Sayo-gun, Hyogo 679-5198, Japan
[e] Department of Materials Engineering, Graduate School of Engineering, The University of Tokyo, 7-3-1 Hongo, Bunkyo-ku, Tokyo 113-8656, Japan

ARTICLE INFO

Article history:
Received 12 July 2012
Accepted 16 September 2012
Available online 8 October 2012

Keywords:
Micelles
Drug delivery
Magnetic resonance imaging (MRI)
Polymer-metal complex
Cancer diagnosis

ABSTRACT

Nanodevices for magnetic resonance imaging of cancer were self-assembled to core–shell micellar structures by metal complex formation of K_2PtCl_6 with diethylenetriaminepentaacetic acid gadolinium (III) dihydrogen (Gd-DTPA), a T_1-contrast agent, and poly(ethylene glycol)-*b*-poly{N-[N′-(2-aminoethyl)-2-aminoethyl]aspartamide} (PEG-*b*-PAsp(DET)) copolymer in aqueous solution. Gd-DTPA-loaded polymeric micelles (Gd-DTPA/m) showed a hydrodynamic diameter of 45 nm and a core size of 22 nm. Confining Gd-DTPA inside the core of the micelles increased the relaxivity of Gd-DTPA more than 13 times (48 mM^{-1} s^{-1}). In physiological conditions Gd-DTPA/m sustainedly released Gd-DTPA, while the Pt(IV) complexes remain bound to the polymer. Gd-DTPA/m extended the circulation time in plasma and augmented the tumor accumulation of Gd-DTPA leading to successful contrast enhancement of solid tumors. μ-Synchrotron radiation-X-ray fluorescence results confirmed that Gd-DTPA was delivered to the tumor site by the micelles. Our study provides a facile strategy for incorporating contrast agents, dyes and bioactive molecules into nanodevices for developing safe and efficient drug carriers for clinical application.

1. Introduction

Early detection of neoplastic lesions is critical for success in cancer therapy. Magnetic resonance imaging (MRI) provides a powerful diagnostic imaging modality of cancer, because of its non-invasiveness, high definition and precise three-dimensional positioning ability [1,2]. Paramagnetic compounds are widely used as MRI contrast agents (CAs) to amplify the signals of MRI tomography and improve the contrast between magnetic similar but histological dissimilar tissues [3,4]. Several low molecular weight paramagnetic complexes of gadolinium(III) are used for clinical MRI as they can decrease the longitudinal relaxation time T_1 of surrounding water protons [5–7]. Among these complexes, Gd-DTPA, one of the most commonly used T_1-contrast agent for clinical MRI, is featured by high thermodynamic and kinetic stabilities, which reduce the release of toxic Gd^{3+} ions, besides a longitudinal relaxivity, r_1, of ~3.5 mM^{-1} s^{-1} at 1.4 T [3,5,7]. Nevertheless, the inherent low relaxivity, short circulation time in blood and low specificity to tissues limit its applications. From this viewpoint, high relaxivity CAs with promoted tissue detection and hindered release of free Gd^{3+} ions are required to improve the performance of imaging.

Nanodevices have been recently developed to selectively deliver imaging agents to solid tumors by leaking out from circulation due to the enhanced permeability of the tumor vasculature [8–12]. In this way, macromolecules, liposomes, dendrimers and nanoparticles carrying high payloads of CAs have been developed to enhance the MR contrast of solid tumors [13–25]. In most cases, Gd-based CAs were covalently incorporated to the structures of nanocarriers to increase the bloodstream circulation, the tumor accumulation and, in some cases, the relaxivity of the loaded CAs

* Corresponding author. Department of Bioengineering, Graduate School of Engineering, The University of Tokyo, 7-3-1 Hongo, Bunkyo-ku, Tokyo 113-8656, Japan. Tel.: +81 3 5841 7138; fax: +81 3 5841 7139.
** Corresponding author. Tel./fax: +81 3 5841 1430.
E-mail addresses: nishiyama@bmw.t.u-tokyo.ac.jp (N. Nishiyama), kataoka@bmw.t.u-tokyo.ac.jp (K. Kataoka).

0142-9612/$ – see front matter © 2012 Elsevier Ltd. All rights reserved.
http://dx.doi.org/10.1016/j.biomaterials.2012.09.030

[14,22,23]. Nevertheless, covalent binding of Gd-chelates to macromolecular systems may increase the risk of Gd^{3+} ion leakage from the chelates due to the prolonged half-life in the body and cumulative toxicity [26]. Thus, the design of tumor-targeted nanodevices for Gd-based CAs should consider such issues for constructing safe carriers, which could target the tumor position and release Gd-DTPA easily from nanodevices.

Among promising nanodevice systems for MRI, block copolymeric micelles, i.e. nanostructures consisting of a drug-loaded core and poly(ethylene glycol) (PEG) protective shell, present exceptional advantages including their relatively small sizes, ability to engineer drug loading mechanisms, controlled release of their cargo, prolonged life in the bloodstream and enhanced accumulation in solid tumors after intravenous administration [19–25]. Auspicious results from clinical trials of micelle formulations incorporating anticancer agents indicate the potential clinical application of polymeric micelles [27,28].

The aim of this study was to develop core–shell type micellar nanocarriers of Gd-DTPA for tumor imaging, which can incorporate Gd-DTPA via the reversible Pt-Gd-DTPA complexation, allowing sustained release of free Gd-DTPA in biological environments. In order to incorporate hydrophilic low molecular weight paramagnetic complexes Gd-DTPA into polymeric micelle, we utilized Pt(IV) ions to "cross-link" carboxyl groups of Gd-DTPA to amino groups of PEG-*b*-PAsp(DET) copolymers. Gd-DTPA/m could passively accumulate in solid tumors due to the enhanced permeability and retention (EPR) effect. Thus, the improved tumor accumulation of Gd-DTPA could enhance the T_1 weighed contrast of the malignancies in mice. Otherwise, in physiological environments such as plasma, the ligand exchange reaction of Pt(IV) from the carboxylic group of Gd-DTPA to chloride ions results in sustained release of free Gd-DTPA, which can be rapidly cleared from the body via glomerular excretion.

2. Materials and methods

2.1. Materials

α-Benzyl-L-aspartate *N*-carboxy anhydride (BLA-NCA) was obtained from Chuo Kaseihin Co., Inc. (Tokyo, Japan). Poly(ethylene glycol) (MeO-PEG-NH_2) (M_w = 12,000, M_w/M_n = 1.03) were purchased Nippon Oil and Fats Co., Ltd. (Tokyo, Japan). Benzene, *N*,*N*-dimethylformamide (DMF), *n*-butylamine, dichloromethane (CH_2Cl_2), diethylenetriamine (DET), potassium hexachloroplatinate(IV) (K_2PtCl_6) and *N*-methyl-2-pyrrolidone (NMP) were purchased from Wako Pure Chemical Industries (Osaka, Japan) and distilled by a general method before use. Arsenazo III and Gd-DTPA were purchased from Aldrich Chemical (Milwaukee, USA), and then Gd-DTPA was converted to sodium salt by adjusting the pH to 7 with NaOH and lyophilization. 400-mesh copper grids were obtained from Nisshin E. M. Spectra/Por-6 membrane was purchased from Spectrum Laboratories (Rancho Dominguez, CA). Dulbecco's modified eagle's medium (DMEM) was obtained from Sigma–Aldrich Co. (St. Louis, USA). Fetal bovine serum (FBS) was purchased from MP Biomedicals, Inc. (Illkirch, France). 96-well culture plates were purchased from Becton Dickinson Labware (Franklin Lakes, USA). The Cell Counting Kit-8 was purchased from Dojindo Laboratories (Kumamoto, Japan).

Murine colon adenocarcinoma 26 (C-26) cells were kindly supplied by the National Cancer Center (Tokyo, Japan). Human umbilical vein endothelial cells (HUVEC), and the endothelial cell growth medium-2 bullet kit (EGM-2 bullet kit) were obtained from Lonza Ltd. (Basel, Switzerland). B16-F10 melanoma cells were purchased from the American Type Culture Collection (Virginia, USA). All the cells are maintained with medium in a humidified atmosphere containing 5% CO_2 at 37 °C. CDF_1 mice (female; 18–20 g body weight; 6 weeks old) were purchased from Charles River Japan (Kanagawa, Japan) and, treated following the policies of the Animal Ethics Committee of the University of Tokyo.

2.2. Synthesis of PEG-b-PAsp(DET)

As shown in Scheme S1, poly(ethylene glycol)-*b*-poly(β-benzyl L-aspartate) (PEG-*b*-PBLA) with different degree of polymerization (DP) (DP = 25, 35, 45) were synthesized by ring-opening polymerization of BLA-NCA initiated by MeO-PEG-NH_2 (M_w = 12,000) according to previously reported method with minor modification [29]. Briefly, BLA-NCA (1.1 g, 4.5 mmol) was dissolved in DMF (2 mL) and then diluted with CH_2Cl_2 (20 mL). MeO-PEG-NH_2 (1.2 g, 0.1 mmol) dissolved in CH_2Cl_2 was added to the solution of BLA-NCA. The reaction was carried out with stirring for 2 days at 35 °C. All the procedures above were under dry argon protection. PEG-*b*-PBLA was collected by precipitating in excess amount of diethyl ether, filtration and vacuumed to dry. In Figure S1, the ^1H NMR spectrum of PEG-*b*-PBLA was measured in d_6-DMSO at 80 °C with a JEOL EX300 spectrometer (JEOL, Tokyo, Japan) using tetramethylsilane (TMS) as an internal standard, and the degree of polymerization (DP = 25, 35, 45) was calculated from the peak intensity ratio of protons both in phenyl groups of PBLA ($C_6H_5CH_2$–, δ = 7.3 ppm) and methylene units (–CH_2CH_2–, δ = 3.6 ppm) of PEG. The polydispersity of PEG-*b*-PBLA was characterized by gel permeation chromatography (GPC) system (HLC-8220, TOSOH Co., Japan) equipped with TSK-gel columns (TOSOH Co., Tokyo, Japan) and an internal refractive index (RI) detector at 40 °C. NMP containing 50 mM LiBr was used as mobile phase with a flow rate of 0.35 mL/min and linear PEG standards were used for calibration. As shown in Figure S2, the GPC chromatogram of the prepared PEG-*b*-PBLA has a unimodal molecular weight distribution (M_w/M_n: 1.03).

PEG-*b*-PAsp(DET) with different DP (25, 35, 45) were prepared separately via aminolysis reaction of PEG-*b*-PBLA with DET following the protocol modified from our former reported method [30]. Briefly, lyophilized PEG-*b*-PBLA (200 mg, 0.01 mmol) was dissolved in NMP (2 mL) and maintained at 5 °C. DET (2.3 mL, 50-equivalent to BLA) was diluted with NMP (2.3 mL) and kept at 5 °C. PEG-*b*-PBLA was added to DET solution and reacted with stirring at 5 °C for 1 h. The reacted mixture was neutralized by 5 M HCl aqueous solution (13 mL, equivalent to the added amino groups) in an ice bath, then dialysis (MWCO: 6000–8000) against 0.01 M HCl aqueous solution, then dialyzed with Milli-Q water under 4 °C. PEG-*b*-PAsp(DET) as the chloride salt form was collected via freeze-dry of final solution. ^1H NMR (D_2O) measurement showed the disappearance of signals belonging to the benzyl group and all the signals featured with PEG-*b*-PAsp(DET) (Figure S3). Degree of polymerization (DP = 25, 35, 45) was calculated by comparing the peak intensity ratio between methylene protons of the α, β-Asp segment (peak f, δ = 2.8 ppm) and methylene units (–CH_2CH_2–, δ = 3.6 ppm) of PEG. GPC measurements of block copolymers were carried out utilizing a HPLC system (JASCO, Japan) equipped with Superdex 75 10/300 GL column (GE Healthcare UK, Ltd.) and UV detector set at 220 nm. The column was eluted with 10 mM AcOH buffer containing 500 mM NaCl (pH 7.4) at a flow rate of 0.5 mL/min at room temperature. The GPC chromatogram of the obtained PEG-*b*-PAsp(DET) was unimodal (Figure S4).

2.3. Preparation of Gd-DTPA-loaded micelles (Gd-DTPA/m)

K_2PtCl_6 (0, 1, 2.5, 5 and 10 mM) was dissolved in Milli-Q water adjusted to pH 7.4 using trace amount of NaOH or diluted in 5 mM PBS buffers, then mixed with Gd-DTPA (5 mM) to incubated at 37 °C for 24 h. PEG-*b*-PAsp(DET) (DP = 25, 35, 45; [DET] = 5 mM) was added to Pt/Gd-DTPA mixture ([Gd-DTPA]/[DET] = 1.0) and incubated at 4 °C for 120 h to spontaneously form Gd-DTPA loaded micelles (Gd-DTPA/m). The micelle was purified by dialysis (MWCO: 6000–8000) against Milli-Q water and ultrafiltration (MWCO: 30,000) to remove free drug and polymer in the solution. Size distribution of the Gd-DTPA/m was evaluated by dynamic light scattering (DLS) measurement at 25 °C using Zetasizer Nano ZS90 (Malvern Instruments, UK). The contents of platinum and gadolinium of micelles were determined by inductively coupled plasma-mass spectrometry (ICP-MS) (4500 ICP-MS; Hewlett Packard, USA).

2.4. Transmission electron microscopy (TEM)

The morphology of micelle was observed on a Transmission Electron Microscope (JEM-1400, JEOL, Japan) operated with 100 kv acceleration voltages and 40 uA beam current. Diluted micelle was stained by mixing with uranyl acetate solution (2%, w/v) and placed on 400-mesh copper grids. The diameters of the core of micelle and size distribution were calculated with Image J, which was designed and provided by National Institutes of Health (NIH). The elements distribution inside micelle was characterized using JEM-2100F (JEOL, Japan) under the scanning transmission electron microscopy (STEM) pattern and scanned by energy dispersive X-ray (EDX) spectra. The specimen for the elements measurements was prepared only loading micelle on 400-mesh copper grids without staining.

2.5. Arsenazo III colorimetric assay

Free Gd^{3+} was determined by the absorption of Gd-Arsenazo III complex referring one arsenazo III method [31]. Briefly, equal molar ratio of arsenazo III solution was mixed with of Gd-DTPA/K_2PtCl_6 mixtures, and then the absorbance spectra were measured using with an UV–vis spectrometer (V-570 UV/VIS/NIR Spectrophotometer, JASCO, Japan) at 660 nm. The absorbance of arsenazo III/$GdCl_3$, arsenazo III/Gd-DTPA, and arsenazo III were measured. All the solutions above were maintained at pH 7.4.

2.6. Release rate of Gd-DTPA from Gd-DTPA/m

The release characterization of Gd-DTPA from the micelle was evaluated by a dialysis method. 1 mL of Gd-DTPA/m solution and 1 mL PBS buffer (20 mM PBS with 300 mM NaCl) were put into dialysis bag (MWCO: 6000–8000) and

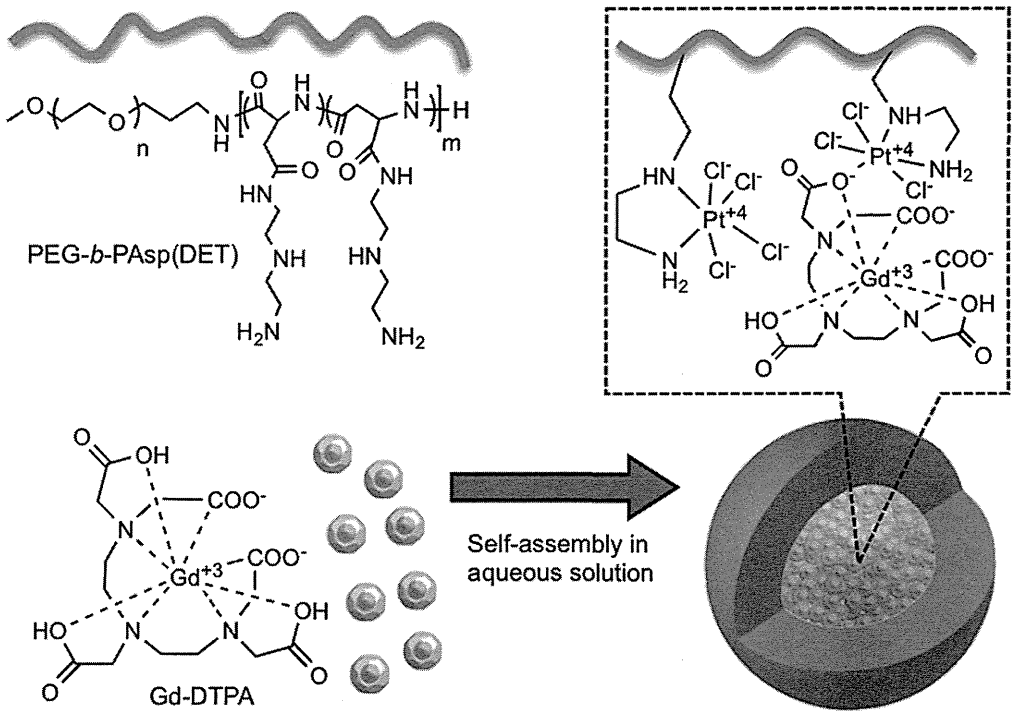

Scheme 1. Scheme illustration of the Gd-DTPA loaded micelle formation via polymer–metal complex formation.

incubated in 98 mL buffer of physiologic conditions (buffer: 10 mM PBS with 150 mM NaCl, temperature at 37 °C). 0.1 mL solution outside of the dialysis bag was sampled at defined time, and then the concentration of Gd-DTPA was measured by ICP-MS.

2.7. Characterization of r_1 relaxivity

The proton longitudinal relaxivity r_1, which is a parameter to evaluate the ability of contrast agents for MRI, can be determined from the change of the relaxation rate

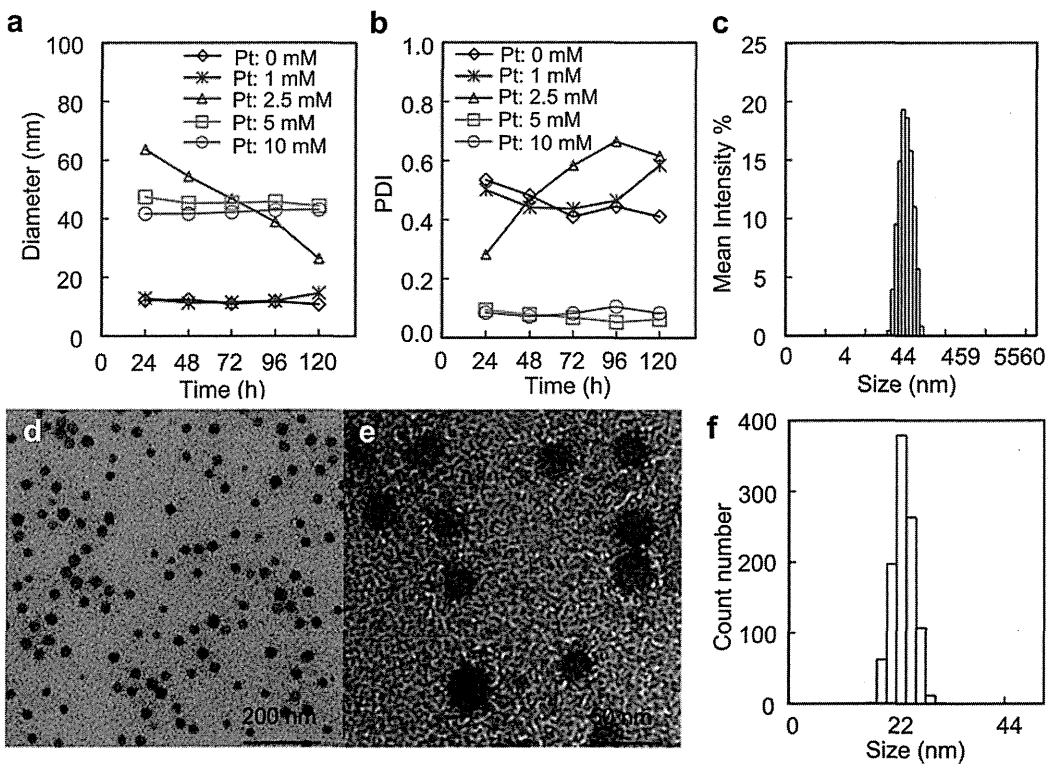

Fig. 1. Change in (a) average diameter and (b) polydispersity index (PDI) of Gd-DTPA/m with different Pt/Gd molar ratios, Gd-DTPA concentration was fixed at 5 mM, and Pt concentration ranged from 0 mM to 10 mM. (c) Size distribution measured by DLS. (d) and (e) TEM of Gd-DTPA/m. (f) Size distribution by number from TEM (n = 1012) calculated from Figure S6.